UCSF

UC San Francisco Previously Published Works

Title

Quantitative surface analysis of combined MRI and PET enhances detection of focal cortical dysplasias

Permalink

Authors

Tan, Yee-Leng
Kim, Hosung
Lee, Seunghyun
et al.

Publication Date

DOI

Peer reviewed

Author Manuscript

Quantitative surface analysis of combined MRI and PET enhances detection of focal cortical dysplasias

Yee-Leng Tan[1,6,*], **Hosung Kim**[2,*], **Seunghyun Lee**[3], **Tarik Tihan**[1], **Lawrence Ver Hoef**[5], **Susanne G Mueller**[4], **Anthony James Barkovich**[4], **Duan Xu**[4], and **Robert Knowlton**[1]

[1]Department of Neurology, University of California, San Francisco, San Francisco, CA

[2]Laboratory of Neuro Imaging, Keck School of Medicine of USC, University of Southern California, Los Angeles, California, USA

[3]Department of Radiology and Biomedical Imaging, University of California, San Francisco, San Francisco, CA

[4]Department of Radiology, Seoul National University Hospital, Republic of Korea

[5]Department of Neurology, University of Alabama, Birmingham

[6]Department of Neurology, National Neuroscience Institute, Singapore

Abstract

Objective—Focal cortical dysplasias (FCDs) often cause pharmacoresistant epilepsy, and surgical resection can lead to seizure-freedom. Magnetic resonance imaging (MRI) and positron emission tomography (PET) play complementary roles in FCD identification / localization; nevertheless, many FCDs are small or subtle, and difficult to find on routine radiological inspection. We aimed to automatically detect subtle or visually-unidentifiable FCDs by building a classifier based on an optimized cortical surface sampling of combined MRI and PET features.

Corresponding Authors: Hosung Kim, PhD, Assistant Professor of Neurology, USC Stevens Neuroimaging and Informatics Institute, Keck School of Medicine of USC, University of Southern California, 2025 Zonal Ave. Los Angeles, CA 90033, Tel: (323) 865-1753, hosung.kim@loni.usc.edu, ghtjdk@gmail.com.
*These authors contributed equally to the manuscript

Methods—Cortical surfaces of 28 patients with histopathologically-proven FCDs were extracted. Morphology and intensity-based features characterizing FCD lesions were calculated vertex-wise on each cortical surface, and fed to a 2-step (Support Vector Machine and patch-based) classifier. Classifier performance was assessed compared to manual lesion labels.

Results—Our classifier using combined feature selections from MRI and PET outperformed both quantitative MRI and multimodal visual analysis in FCD detection (93% vs 82% vs 68%). No false positives were identified in the controls, whereas 3.4% of the vertices outside FCD lesions were also classified to be lesional ("extralesional clusters"). Patients with type I or IIa FCDs displayed a higher prevalence of extralesional clusters at an intermediate distance to the FCD lesions compared to type IIb FCDs (p<0.05). The former had a correspondingly lower chance of positive surgical outcome (71% vs 91%).

Conclusions—Machine learning with multimodal feature sampling can improve FCD detection. The spread of extralesional clusters characterize different FCD subtypes, and may represent structurally or functionally abnormal tissue on a microscopic scale, with implications for surgical outcomes.

Introduction

Focal cortical dysplasias (FCDs) are a type of malformation of cortical development, and are histologically subtyped based on the alterations in cortical lamination (type I) and presence of dysmorphic neurons with or without balloon cells (type II).[1] They are intrinsically epileptogenic, and are a well-recognized cause of pharmacoresistant epilepsy in both children and adults.[2] Surgical resection can lead to seizure-freedom.

The MRI features of FCDs may include cortical thickening, blurring of the grey-white matter junction, an abnormal sulcal or gyral pattern, focal hypoplasia, T2 hyperintense signal within the dysplastic lesion relative to normal cortex, and a decreased T1/increased T2 signal extending from the ventricle to the cortex (transmantle sign, seen in type II FCDs).[3] Yet many FCDs are small or subtle, and are difficult to visually identify on MRI. In fact, histopathology studies have shown that up to 40% of type II FCD and 85% of type I FCD are reported to be MRI-negative on visual inspection,[4,5] being variably dependent upon the imaging technique and the experience of the interpreter.

When the MRI is unrevealing, 2-[^{18}F]fluoro-2-deoxy-D-glucose (FDG)-PET is performed to help with localization of epileptogenic disturbances in metabolism, which may aid identification of occult FCDs that are missed on MRI. FDG-PET often reveals focal hypometabolism in the FCD region, and has been shown to have a diagnostic sensitivity of 78–83% in FCD detection.[6,7] This sensitivity increases further with the use of PET/MRI coregistration.[4]

Since identification of an epileptogenic focus on neuroimaging is a positive predictor for surgical success,[8] MRI post-processing tools have been developed to improve the diagnostic yield of FCDs. Voxel-based morphometric and texture analyses[9,10,11] have successfully characterized quantitative features of FCD lesions. Surface-based feature sampling and classification based on lesion characteristics along the cortical folds have further improved the accuracy of FCD detection.[12,13,14,15] These techniques have helped to convert many "lesion-negative" MRIs into "lesion-positive" cases.[12,13] The advantages of combining quantitative MRI and PET in FCD detection remain to be explored.

Here, we built a classifier based on an optimized cortical surface sampling of combined MRI and PET quantitative features, for the detection of FCDs that were subtle or visually-negative even after multimodal imaging evaluation. To optimize both feature modeling and classification, we integrated a framework of patch library construction and label fusion that has been widely used for brain structural segmentation,[16,17,18] into a surface-based classification. We also endeavored to establish the clinical utility of this classifier by testing its performance on patients with histopathologically-confirmed FCDs, while using patients with MRI-negative temporal lobe epilepsy (TLE) as a reference group.

Methods

The overall procedure of the proposed classification approach is shown in Figure 1.

Patient selection

We retrospectively identified 28 patients who had undergone surgical resection for localization-related medically refractory epilepsy, with histopathological confirmation of FCD from our surgical databases at two institutions (University of California, San Francisco [UCSF]; n=12, and University of Alabama, Birmingham [UAB]; n=16), over a 10-year period (2005–2015). The pathology specimens were reviewed by a pathologist (T.T.) and subtyped under the International League Against Epilepsy (ILAE) classification. Patients were included if they had a pre-surgical 3.0 Tesla MRI with three-dimensional (3D) T1-weighted sequence, as well as pre-surgical 3D FDG-PET. The following patients were excluded: (i) poor image quality scans (due to motion artifact, aliasing or rippling related to eye movement), (ii) age<2 years old (due to incomplete myelination), (iii) type III FCD on histopathology (e.g. FCD with another principle lesion such as hippocampal sclerosis), (iv) large/diffuse FCDs on MRI, and (v) more than one FCD lesion visible on MRI. Patients with multiple visible FCDs were excluded as it was possible these patients had tuberous sclerosis complex, reflecting a different genetic etiology. Also, as the remaining FCDs had potential epileptogenicity, this could affect the surgical outcomes. The patient demographics and lesion characteristics are summarized (Table 1). We used pre-surgical MRI and FDG-PET scans from 23 patients with MRI-negative TLE as a reference ("control") group, as it is not practical to obtain healthy controls imaged using both modalities in the clinical setting. We had intracranial electroencephalogram (ICEEG) confirmation of seizures arising from mesiotemporal regions. All MRI-negative TLE patients chosen for the current study underwent epilepsy surgery and hence had histopathological verification of the absence of FCD. Their histopathology findings are shown in Table 1.

FCD patients were followed up post-operatively for a mean period of 15.6 (±16.6) months. At their last documented visit, 76.8% had good (Engel I and II) surgical outcomes. This study was approved by the ethics committees of both UCSF and UAB.

MRI and FDG-PET acquisition

All images were acquired at 3.0T field strength using dedicated MRI epilepsy protocols. 3D T1-weighted IR prepped gradient echo scan sequences were used for quantitative image analysis, and their parameters are described (Table S1). In addition, fluid-attenuated inversion recovery (FLAIR) images (slice thickness 1–4mm), and T2-weighted images (thickness 1–3mm) were included as part of the clinical protocol, complementing qualitative image interpretation. Acknowledging the importance of thin FLAIR slices in the clinical identification of small lesions, both institutions (UCSF and UAB) routinely used 1mm volumetric coronal acquisitions after 2011. Prior to this, FLAIR sequences were 3mm thick, and anything above this was an exception.

FDG-PET scans were acquired in the interictal state under standard resting conditions (eyes closed, dimmed ambient light) using CTI ECAT HR+, GE-Discovery LS, and GE-Discovery STE PET/CT scanners. Approximately 45 minutes following the intravenous administration of 2.6–13.2 mCi 18F-labeled FDG, 3D PET images of the brain were obtained from the vertex to skull base (slice thickness 3.0–4.25mm). Images were attenuation-corrected using noncontrast CT transmission information.

Image processing and cortical surface construction

Intra-subject PET and MR images were co-registered using a mutual information-based rigid-body transformation (mri-to-self in minc tool package).[19] The CIVET pipeline (version 1.1.12; http://www.bic.mni.mcgill.ca/ServicesSoftware/CIVET1112) was performed on T1-weighted structural images to spatially normalize the brain size, segment brain tissues and generate a model of the GM-WM and GM-CSF surfaces. The pipeline first automatically performed correction for intensity nonuniformity and intensity standardization, linear registration into standardized stereotaxic space (defined using MNI-ICBM 152 template, version 2009c), and automatic classification of T1-weighted images into white matter (WM), gray matter (GM), and CSF. Deformable models were then used to construct the WM-GM and GM-CSF interfaces in both hemispheres.[20] These yielded 40,962 vertex points per surface. Extracted surfaces were nonlinearly aligned to the surface template using a 2D registration procedure based on patterns of cortical folding that improves inter-individual correspondence.[21] The accuracy of surface extraction was validated by visual inspection.

FCD feature extraction from MRI

At each vertex of the surface, we calculated morphology (cortical thickness and sulcal depth) and intensity-based (GM relative intensity, gradient at GM-WM interface) features representing the lesional characteristics of FCDs. The features were extracted at a different level of the cortical depth depending on the given feature. The details are described below:

Morphological features: i) cortical thickness measured as the shortest distance between corresponding vertices on the WM-GM and GM-CSF surfaces; ii) sulcal depth (it was

previously shown that small lesions were located at the bottom of a deep sulcus)[14] was defined as the geodesic distance between the given vertex located within sulci and the closest vertex within the gyral crown which was defined as the vertices showing larger than zero in the depth potential measurement.[22]

Intensity features: i) relative intensity (RI) was measured in a similar manner as previously described by Hong et al.,[12] and defined as $RI(x) = 100 \times (I(x) - I_{GM\_peak})/(B - I_{GM\_peak})$, where $I(x)$ is the intensity at voxel x, I_{GM_peak} the intensity of GM peak obtained from the whole-brain histogram, and B the intensity at the boundary between GM and WM. Three equidistant intracortical surfaces were created by placing uniformly spaced vertices between linked vertices of GM-WM and GM-CSF surfaces. The RI was then interpolated at each vertex of these surfaces and averaged; ii) gradient (blurring / low gradient at the GM-WM interface has characterized FCD lesions) was computed as intensity differences between 0.5 mm above and below the GM-WM interface along the surface normal vector. Note that the denominator of the gradient is uniformly 1 across all vertices.

MRI and PET features were computed after first warping surfaces back first into each subject's MRI native space, and subsequently into PET native space by inversely transforming the previously performed PET-to-MRI registration. These features were then resampled on the MNI-ICBM surface template using the related transformation.

FCD feature extraction from PET

Cortical PET intensities were sampled using mid surfaces (i.e., the 2nd intracortical surface generated previously) to avoid possible partial volume effects between different brain tissues. The following features were extracted: i) normalized intensity at a given vertex (nPET) was used to characterize the hypointensity of each FCD lesion. This feature was measured as $nPET(x) = 100 \times (PET(x) - PET_{CSF\_vent})/(PET_{WM\_peak} - PET_{CSF\_vent})$, where $PET(x)$ is the PET intensity at x, PET_{CSF_vent} the intensity of CSF peak obtained from the histogram of the lateral ventricle, and PET_{WM_peak} the intensity of WM peak obtain from the whole histogram; ii) hemispheric asymmetry (aPET) was used to capture the relatively lower PET intensity in the FCD lesion compared to its homotopic location in the contralateral brain hemisphere (which was assumed to be non-lesional), even though the net lesional intensity itself may not be abnormal. This feature at a given vertex x was measured as $aPET = 2 \times (L(x) - R(x))/(L(x) + R(x))$, where L / R denotes left / right. We mapped aPET when x is a voxel on the left hemisphere, and –aPET when x is on the right in order to identify a hypointensity in the correct hemisphere.

Feature smoothing and normalization

Prior to classification, features were smoothed using a 5-mm full-width-at-half-maximum (FWHM) Gaussian surface kernel. This small-size kernel was used for the detection of small / MRI-negative lesions in a previous study[12] and was proven to yield high sensitivity. Each type of feature was then normalized: To account for the large age range of our dataset, we first normalized each type of feature across all the vertices within a given individual using z-score normalization (intra-subject normalization); feature values at a given vertex

were then normalized with respect to the distribution of the TLE group using z-score normalization (inter-subject normalization).

Lesion labeling

FCD lesions were labeled by two imaging physicists (S.L. & H.K.) who were trained in imaging characteristics of FCDs. We measured their inter-rater agreement using kappa-statistics (inter-rater agreement: $\kappa = 88 \pm 5\%$ for all cases). Even though this agreement was considered "excellent", raters may not always yield consistent labels at the level of the "gold" standard. Thus, in addition, two neurologists with extensive neuroimaging expertise (Y-L.T. & R.K.) reviewed the segmentations using imaging features in combination with seizure history, clinical examination, and video EEG. For optimal segmentation, raters and reviewers reached a consensus in labeling each individual FCD lesion for all cases. For FCD lesions that were not visible on MRI scans at the first examination, the lesion locations were identified based on the locations of surgical cavities in post-surgical scans. When we revisited these locations, we could find the presence of small size FCDs in pre-operative scans, and successfully outlined them using combined MRI and PET imaging characteristics. This volumetric label was projected onto cortical surfaces, and blurred with a kernel of 5mm FWHM, which was the same as the kernel used for feature smoothing. The probabilistic map of lesion labels is shown in Figure S1.

Lesion characteristics

In patients, we averaged each quantitative feature within the lesion label. These values were displayed using box-whisker plots for each histopathological FCD subtype.

Optimization of classification

Automated classification of lesional versus non-lesional tissue types was performed in two steps. The first step in which we applied the Suport Vector Machine (SVM)-based classifier was designed to recognize lesional vertices with the highest detection rate. Starting within the detected lesional areas, we then carried out the patch-based classifier to remove false positives (FP) generated by the first classifier. Details are found below:

Similar to previous quantitative studies,[12,15] we first employed a linear classifier. We adopted the SVM classifier that uses the support vectors as representative points in the feature space so that these points of the different classes are divided by a clear gap that is as wide as possible. As our features were constructed based on hypotheses, they should explain intuitively the imaging characteristics of FCD lesion. We then adopted a patch-based classifier (Figure 1B). This approach, adapted for the surface feature analysis in the current study, determined a label (i.e., lesional or non-lesional) corresponding to a given vertex $\mathbf{x}_t$ on the target cortical surface according to the similarity between its surrounding patch $P(\mathbf{x}_t)$ and all the patches $P(\mathbf{y}_s)$ taken from training surfaces (s | s=$1,2,\ldots,N$) in the library (= training-set).

A training vertex $\mathbf{y}_s$ was selected inside a search area ($\mathbf{y} \in \eta_{xt}$). In other words, for the patch P centered at the vertex $\mathbf{x}_t$ of the target surface, similar patches extracted from the N surfaces were searched for within the neighborhood η_{xt}. We defined the smallest patch as an

aggregation of vertices that form 6-connected neighbors on the triangulated surface. A 6^2-connected neighbor was defined as the aggregation of the given neighboring 6-connected vertices. In the same way, a 6^n-connected neighbor was defined using the 6^{n-1}-connected neighbors. Using a method previously introduced by Eskildsen et al,[23] we calculated the probability of the label at the vertex $\mathbf{x}_t$ using the nonlocal mean estimator and the similarity measure between the target patch $P(\mathbf{x}_t)$ and the library patch $P(\mathbf{y}_s)$. As introduced in the original study by Coupe et al,[16] we calculated the probability of the label at the vertex $\mathbf{x}_t$ using the nonlocal mean estimator $v^l(x_t)$:

$$v^l(x_t) = \frac{\sum_{s=1}^{N}\sum_{y\in\eta} w_l(x_t, y_s) l(y_s)}{\sum_{s=1}^{N}\sum_{y\in\eta} w_l(x_t, y_s)} \quad (1)$$

Where $l(\mathbf{y}_s)$ is the label of vertex $\mathbf{y}$ on the current template surface s. For the purpose of FCD detection, we define the label values as background = 0, and FCD = 1. The weight $w_l(x_t, y_s)$ of the label $l(\mathbf{y}_s)$ was computed based on the similarity between patches $P(\mathbf{x}_t)$ and $P(\mathbf{y}_s)$ as:

$$w_l(x_t, y_s) = e^{\frac{\|P(x_t) - P(y_s)\|_2^2}{h}} \quad (2)$$

$|\bullet\|_2$ is the normalized L2 norm that is normalized by the number of patch elements and computed between each intensity of the elements of the patches $P(\mathbf{x}_t)$ and $P(\mathbf{y}_s)$. The parameter h is locally adapted using the minimal distance between the target patch and the template patches.[16]

The lesion label was determined at a given threshold of probability (i.e., a probability above the threshold labeled $\mathbf{x}_t$ as "lesional"). We determined the search area $\mathbf{y}$ as the lobe (parcelled by a surface-based approach)[24] that the target vertex $\mathbf{x}_t$ belonged to, and the mirror lobe in the contralateral hemisphere. In this manner, we sufficiently sampled the lesional patches in the library, regardless of the location of $\mathbf{x}_t$. For each classification step, we trained and cross-validated the classifier using a leave-one-out strategy. This was based on the subjects and not based on the vertex samples. In other words, for testing of each individual subject, we used all subjects minus that subject to construct the training-set. This procedure was equally applied for the 2 step-wise classifiers.

Sampling non-lesional tissue

We defined "non-lesional tissue" for the classification process by sampling tissue from cortical regions in the TLE subjects. However, TLE subjects could potentially harbor extratemporal cortical abnormalities including cortical thinning[25] and PET hypometabolism.[26] We thus also sampled tissue from extralesional areas in FCD patients, and compared the classification performance based on these two different sampling schemes (TLE vs FCD-extralesional).

Evaluation of classification accuracy

We defined a lesion detection rate as the proportion of FCD patients in whom a detected cluster overlapped with the manual lesion label. We computed specificity as the proportion of TLE subjects in whom no lesion cluster was falsely identified. True positive (TP) coverage was defined as the proportion of detected cluster area which overlapped with the manual label. False positive (FP) rate per individual was defined as the number of vertices of FP / number of vertices of negative vertices (true negative [TN] + false negative [FN]).

Results

Lesion characteristics (Figure 2)

In type IIb FCD (n=14), all examined features known to be characteristic of FCDs were significantly abnormal compared to TLE subjects (p-values were corrected using Bonferroni adjustment) - cortical thickening (z-score: 2.4±1.8; t=5.0; p<0.001;, unless otherwise specified), sulcal deepening (i.e., z: 2.6±2.9; t=3.6; p<0.05), GM-WM blurring (i.e., low gradient; z: −1.7±1.6; t=3.8; p<0.01), GM hyperintensity (i.e., higher RI; z: 1.7±1.9; t=3.4; p<0.05), PET hypointensity (i.e., low nPET; z: −1.4±1.1; t=3.8; p<0.01), and low PET signal compared to its mirror site in the opposite hemisphere (aPET: z: −1.7±1.3; t=3.8; p<0.01).

In type IIa FCD (n=11), only PET hypointensity (z: −1.8±1.4; t=4.4; p<0.001), and aPET (z: −2.2±1.6; t=4.7; p<0.0005) significantly characterized lesional abnormalities. We found a trend of cortical thickening (z: 1.5±2.2; t=2.6; p=0.02 uncorrected) and blurring (z: −1.3±1.2; t=3.0; p=0.005 uncorrected) in these lesions. Neither GM intensity nor sulcal depth was different from TLE subjects (p>0.1). The multivariate Hotelling T^2-test showed that the MRI features were significantly different between type IIa and IIb FCD groups (T^2=8.1; p<0.01) whereas the PET features did not differ (T^2=2.3; p>0.2).

Imaging abnormalities in type I FCD were not found to be significant due to the small sample size (n=3). Nonetheless they showed features of cortical thickening (z: 1.4±1.5), shallow sulcation (z: −0.5±0.4), GM-WM blurring (z: −1.9±2.4), GM hyperintensity (z: 1.6±2.8), PET hypointensity (z: −2.1±2.3), and low PET intensity compared to the mirror site (z: −0.8±1.1).

Parameters selection

The highest sensitivity and specificity was obtained for the patch-based classifier using a search area **y** as the 6^5-connected neighbor or larger, and the patch size **P** as the 6^2-connected neighbor or larger. Use of the threshold of 46% label probability resulted in the best performance as we obtained the highest TP detection rate (up to 93%) with very low FP rates in TLE subjects (0.1%; Table 2) and when sampling "extralesional" tissue (0.3%; Table 3).

Classification performance

Sampling nonlesional tissue from TLE subjects yielded superior results as compared to sampling "extralesional" tissue from FCD patients (see Table 3) as a normal reference, and are described below.

Step 1 (Table 2A): When analyzing classifier performance based on MRI-alone vs combined MRI and PET (MRI+PET) features, we found the best trade-off between the sensitivity and specificity at the posterior probability of 91% in the SVM classifier, in which we obtained the highest TP and lowest FP rates. MRI+PET analysis detected all FCD lesions (28/28=100%) whereas analysis using MRI-alone missed one lesion (27/28=96%). Classification using MRI+PET also demonstrated a lower FP rate in TLE subjects (1.1% lower; t=3.0; p<0.005) compared to MRI-alone analysis. On the other hand, use of MRI +PET revealed a larger FP rate in FCD patients compared to MRI-alone (4.3% higher; t=1.8; p=0.1). The relatively high FP rate in FCD patients was present even at the highest posterior probability (99%) where a very low FP rate in TLE subjects was found (MRI-alone: 1.4%; MRI+PET: 0.6%), suggesting the presence of extralesional pathology in the FCD group. At the maximum posterior probability, MRI+PET also showed a higher sensitivity in FCD lesion detection than MRI-alone (89% *vs.* 79%).

Step 2 (Table 2B): Compared to the SVM in step 1, the patch analysis particularly improved the specificity, resulting in 0% FP rate in the TLE reference group (*vs.* 1.6±0.9; t=9.8; p<0.00001) when using MRI+PET while maintaining a high TP detection rate (26/28=93%). Similar to the results obtained in step 1, when compared to MRI-alone analysis, MRI+PET demonstrated a higher TP detection rate (93% vs. 82%), lower FP rate in TLE subjects (0% vs. 0.1%) and detection of more extralesional abnormalities in FCD patients (3.4% vs 2.5% vertices). This trend was also seen at the highest probability threshold (99%).

Classification performance when sampling "extralesional" tissue from FCD patients as reference

The overall results are shown in Table 3. Through classification steps 1 and 2, lesion detection rate dropped by 9%–14% compared to sampling nonlesional tissue from the TLE group. While the FP rate was lower in FCD patients (FCD: 0.5–4.2%) compared to sampling from TLE, it was slightly increased in the TLE group (TLE: 0.1–0.2%). Extralesional abnormalities were still found throughout the classification steps 1 and 2. Moreover, FP clusters in the TLE subjects were still detected even after running the 2nd classifier, suggesting that sampling nonlesional tissues in FCD patients would be less optimal than sampling non-FCD epilepsy subjects.

Subsequent analysis of extralesional FCD clusters

Despite having zero-FP rate in the TLE group, the classifier identified lesional vertices outside the known FCD lesion (3.4±1.2%). These extralesional abnormalities were located significantly more frequently in the hemisphere ipsilateral to the lesion (ipsi: 2.9±1.3 vs. contra: 0.5±1.3%; t=9.2; p<0.00001). To assess the proximity of extralesional clusters to the primary lesion, the geodesic distance from the boundary of the lesion label to each extralesional vertex was measured, and their distance maps plotted (Figure 3). To measure the distance from the lesion to the contralateral hemisphere, we first projected the lesion on this hemisphere surface based on the hemispheric point-correspondence. The distance in the contralateral hemisphere was then computed with respect to this projected lesional mask.

The largest population of extralesional clusters was perilesional (1–30mm; 339 vertices per patient), the 2nd largest was closely located within the same ipsilateral lobe or neighboring lobes (40–80mm; mean=202 vertices), and the 3rd largest was within the same lobe in the contralateral hemisphere (30–60mm; 132 vertices). Patients with type I or IIa FCDs displayed a larger number of extralesional vertices than those with type IIb in the 40–80mm distant region (#vertices: 351±288 *vs.* 142±137; p<0.05). These patients had a lower proportion with good surgical outcomes compared to the type IIb FCD group (71% vs. 91%). The probabilistic mapping of the extralesional clusters (Figure S2) showed that they were mainly located in the proximity of their corresponding primary lesions (Figure S1). This was in keeping with the information shown in Figure 3. Although the extralesional clusters were more prevalent in the ipsilateral rather than contralateral hemisphere, the pattern of extralesional clusters was however very symmetric between hemispheres, with regions of high probability (>10%) seen in the orbitofrontal, inferior prefrontal, cingulate, temporal pole and central cortices.

Comparison between visual and quantitative methods for FCD identification (Table 4)

Both quantitative methods using MRI-alone or MRI+PET showed significantly higher sensitivity for FCD detection relative to their respective multimodal visual evaluation (Fisher's exact tests; p<0.05). Significantly higher sensitivity for the MRI+PET quantitative method was achieved in patients with type I (visual: 67% vs. quantitative: 100%; p=0.1) and type IIa FCD (24% vs. 91%; p=0.003).

Discussion

Quantitative FCD detection methods have consistently shown higher sensitivities compared to qualitative visual analysis.[12,27,28] To date, these analyses have been applied only to single imaging modalities (MRI or PET), although PET scans can aid localization of the epileptogenic zone when the MRI is visually negative.[29] In our study, we took advantage of the availability of PET scans, and demonstrated superior sensitivity in FCD detection using feature modeling of combined MRI and PET, compared to quantitative MRI alone. Our PET +MRI quantitative classifier was also more sensitive than routine visual radiological examinations of MRI and PET, proving its value in FCD lesion identification. Further, the classifier revealed extralesional abnormalities in FCD patients, with pattern differences between FCD subtypes. To the best of our knowledge, the quantitative analysis of *combined* PET and MRI is indeed new in FCD detection. Even though our pipeline is a two-stage classifier similar to our previous work [12], a significant improvement was made by adapting the nonlocal patch featuring and label fusion method to a surface approach of detecting FCD lesions. Furthermore, our sampling of PET features on the mid-cortical surface advances conventional volumetric approaches by minimizing the partial volume effects.[30] Lastly, the analysis in depth with respect to the extralesional clusters and the relationship with the surgical outcome has not been investigated prior to the current study.

Excellent classifier performance despite scanner heterogeneity

The MRI and PET images used in the current study were clinical scans conducted during the course of the patients' presurgical evaluation. We performed the classification using a leave-

one-out approach to avoid bias related to the training process. Our image data acquired in routine clinical scanners however inevitably contained mild variations in data resolution, with subsequent different degrees of partial volume effects as shown in Table S1. Also, the size of the training-set was not considerably large although the size of the samples in our study was one of the largest in the FCD detection algorithms to date.[12,13] Such weaknesses might have resulted in overfitting and potentially boosted our excellent classification performance. Further analysis will help clarify the effects of such variations on the classification process. The accurate classification in the current study is however in keeping with a previous study that documented equivalent cross-validation performances in classifiers trained on images acquired with both homogeneous and heterogeneous hardware settings.[31] These findings encourage transition of this method to clinical application in other institutions, especially where high-level visual interpretation expertise is not available.

The use of TLE subjects as a reference group

Whole-brain PET imaging involves exposure to ionizing radiation, and it is difficult to find healthy subjects with PET images who are free of central nervous system disease in the clinical setting. MRI-negative TLE subjects who exhibited no dual pathology and who had undergone both MRI and PET imaging were chosen as a reference group in our study as they most closely matched the age range of FCD patients, and were used to provide feature standardization.

MRI features in TLE are known to be quite different from FCD subjects, as widespread cortical thinning in even MRI-negative TLE patients has been reported,[25] as opposed to the cortical thickening seen in FCD lesions. Although hypometabolism in the epileptogenic temporal lobes and perhaps also in extra-temporal regions in TLE subjects rendered them suboptimal as PET control scans, the excellent performance of our classifier may be explained by its multivariate analysis of MRI+PET features. Of note, all four temporal lobe FCDs were successfully detected.

The performance of our classifier using TLE subjects as reference shows that it is possible for other clinical centers to adapt this methodology for FCD detection without the necessity of scanning healthy subjects. We specifically chose to test TLE patient scans as controls since these scans would be available in the typical clinical environment; the ease of translating this methodology for widespread institutional use being an important goal of this work.

Lesional characteristics by histological subtypes

FCD type IIa lesions are more difficult to diagnose using conventional visual analysis compared to type IIb, due to their milder MRI abnormalities.[32] Indeed, all the MRI features were observed to be significantly abnormal in our type IIb lesions, whereas type IIa lesions only showed PET hypointensity and asymmetry, with a trend towards cortical thickening and GM-WM junction blurring. Importantly, in the type IIa group the classifier had the highest yield in converting "non-lesional" cases to "lesional" ones, as multivariate analysis of PET and MRI features, although subtle, boosted the detection power. A larger sample size is needed for conclusive lesion characterization of type I FCDs.

Extralesional clusters in FCD patients

Extralesional clusters were identified in 3.4% of the vertices in FCD patients. The phenomenon of extralesional cluster detection in FCD patients is not new.[12,33] Both our classifier and a previous study[12] identified none or very limited false positive clusters in TLE subjects. Furthermore, sampling "nonlesional tissues" from FCD patients did not entirely remove the presence of extralesional clusters after the 2nd classification step, while we observed a decrease in the FCD detection rate. This suggests the existence of extralesional abnormalities that resemble the feature characteristics of the FCD lesion, and consequently, likely reflect subtle multifocal FCDs. In fact, nineteen percent of small FCDs have been reported to be multilobar in location[32]; and although multilobar FCDs were excluded from our study by visual analysis, microscopic variants could have escaped detection.

We also investigated the proximity of extralesional abnormalities to the primary lesion, and its relationship with FCD histopathological subtypes and surgical outcome. Extralesional clusters were located most preferentially in perilesional locations, followed by locations within the same or neighbouring lobes within the same hemisphere. This finding is corroborated by a study which examined the MRI characteristics of multi-focal FCDs,[34] and found 80% of the lesions to occur within the same hemisphere.

Finally, patients with type I or IIa FCD had a lower chance of good surgical outcomes (70 vs 91%) compared to those with type IIb FCD, and displayed a correspondingly larger population of extralesional clusters. This suggests that extralesional clusters may be potentially epileptogenic, which could explain why not all patients with complete resection of the primary FCD lesion become seizure-free.[35]

Interestingly, the contralateral extralesional clusters were seen to be in the homotopic lobe as the primary lesion and the pattern of these clusters was very similar to that of the ipsilateral extralesional clusters. Such a contralateral abnormality has also been found in previous studies,[11,12] which may explain the developmental characteristics of FCDs. The epileptogenic nature of this abnormality is however unclear as its presence did not necessarily worsen the surgical outcome in our analysis.

Technical consideration

Some studies reported abnormal sulcal patterns in FCD compared to healthy controls.[36,37,38] The abnormal sulcal patterns observed in these previous studies may have influenced our 2D surface registration that used a sulcal morphological property (i.e., sulcal depth potential) and a template constructed based on a healthy population (MNI-ICBM 152). This issue may need further investigation to be fully addressed. However, it is worth noting that the extent of abnormal sulcal shapes in FCD observed in the aforementioned studies is relatively small with a nature of branching out of a main sulcal body. The impact of mis-registration due to this would be focal. It is also noted that the MNI-ICBM template has been used in numerous clinical studies dealing with the brain diseases or disorders where abnormal sulcation patterns are implied.[39,40,41] On the other hand, a smoothing procedure has been adopted in the registration to address such morphological variability. We followed a standard size of the

smoothing kernel.[21] The focal nature of the sulcal abnormality and a smoothing of sulcal feature in the registration may therefore explain, at least partly, the maintained high performance of the FCD identification in our classification.

Conclusion and future directions

We present an objective, quantitative classifier combining features from both MRI and PET imaging, with a high sensitivity and specificity in FCD lesion detection. This method is superior to both conventional visual analysis and single modality quantitative analysis. Although the current classification result obtained using TLE subjects as a group reference was very satisfactory, use of healthy controls will better clarify the results and the nature of detected abnormalities. We intend to continue refining and testing the methodology for diagnostic accuracy, and once validated on prospective subjects, we hope to develop a software pipeline which incorporates these methods into a software for distribution.

Supplementary Material

Refer to Web version on PubMed Central for supplementary material.

References

1. Blumcke I, Thom M, Aronica E, et al. The clinicopathologic spectrum of focal cortical dysplasias: a consensus classification proposed by an ad hoc Task Force of the ILAE Diagnostic Methods Commission. Epilepsia. 2011; 52(1):158–174. DOI: 10.1111/j.1528-1167.2010.02777.x [PubMed: 21219302]

2. Semah F, Picot MC, Adam C, et al. Is the underlying cause of epilepsy a major prognostic factor for recurrence? Neurology. 1998; 51(5):1256–1262. [PubMed: 9818842]

3. Widdess-Walsh P, Diehl B, Najm I. Neuroimaging of focal cortical dysplasia. J Neuroimaging. 2006; 16(3):185–196. DOI: 10.1111/j.1552-6569.2006.00025.x [PubMed: 16808819]

4. Salamon N, Kung J, Shaw SJ, et al. FDG-PET/MRI coregistration improves detection of cortical dysplasia in patients with epilepsy. Neurology. 2008; 71(20):1594–1601. DOI: 10.1212/01.wnl. 0000334752.41807.2f [PubMed: 19001249]

5. Mellerio C, Labeyrie M-A, Chassoux F, et al. Optimizing MR imaging detection of type 2 focal cortical dysplasia: best criteria for clinical practice. AJNR Am J Neuroradiol. 2012; 33(10):1932–1938. DOI: 10.3174/ajnr.A3081 [PubMed: 22555587]

6. Kim YH, Kang H-C, Kim D-S, et al. Neuroimaging in identifying focal cortical dysplasia and prognostic factors in pediatric and adolescent epilepsy surgery. Epilepsia. 2011; 52(4):722–727. DOI: 10.1111/j.1528-1167.2010.02950.x [PubMed: 21275980]

7. Chassoux F, Rodrigo S, Semah F, et al. FDG-PET improves surgical outcome in negative MRI Taylor-type focal cortical dysplasias. Neurology. 2010; 75(24):2168–2175. DOI: 10.1212/WNL. 0b013e31820203a9 [PubMed: 21172840]

8. Lee SK, Lee SY, Kim K-K, Hong K-S, Lee D-S, Chung C-K. Surgical outcome and prognostic factors of cryptogenic neocortical epilepsy. Ann Neurol. 2005; 58(4):525–532. DOI: 10.1002/ana. 20569 [PubMed: 16037972]

9. Huppertz H-J, Grimm C, Fauser S, et al. Enhanced visualization of blurred gray-white matter junctions in focal cortical dysplasia by voxel-based 3D MRI analysis. Epilepsy Res. 2005; 67(1–2): 35–50. DOI: 10.1016/j.eplepsyres.2005.07.009 [PubMed: 16171974]

10. Antel SB, Bernasconi A, Bernasconi N, et al. Computational models of MRI characteristics of focal cortical dysplasia improve lesion detection. Neuroimage. 2002; 17(4):1755–1760. [PubMed: 12498749]

11. Colliot O, Bernasconi N, Khalili N, Antel SB, Naessens V, Bernasconi A. Individual voxel-based analysis of gray matter in focal cortical dysplasia. Neuroimage. 2006; 29(1):162–171. DOI: 10.1016/j.neuroimage.2005.07.021 [PubMed: 16099679]

12. Hong S-J, Kim H, Schrader D, Bernasconi N, Bernhardt BC, Bernasconi A. Automated detection of cortical dysplasia type II in MRI-negative epilepsy. Neurology. 2014; 83(1):48–55. DOI: 10.1212/WNL.0000000000000543 [PubMed: 24898923]

13. Ahmed B, Brodley CE, Blackmon KE, et al. Cortical feature analysis and machine learning improves detection of "MRI-negative" focal cortical dysplasia. Epilepsy Behav. 2015; 48:21–28. DOI: 10.1016/j.yebeh.2015.04.055 [PubMed: 26037845]

14. Besson P, Andermann F, Dubeau F, Bernasconi A. Small focal cortical dysplasia lesions are located at the bottom of a deep sulcus. Brain. 2008; 131(Pt 12):3246–3255. DOI: 10.1093/brain/awn224 [PubMed: 18812443]

15. Besson P, Bernasconi N, Colliot O, Evans A, Bernasconi A. Surface-based texture and morphological analysis detects subtle cortical dysplasia. Med Image Comput Comput Assist Interv. 2008; 11(Pt 1):645–652. [PubMed: 18979801]

16. Coupe P, Manjon JV, Fonov V, Pruessner J, Robles M, Collins DL. Patch-based segmentation using expert priors: application to hippocampus and ventricle segmentation. Neuroimage. 2011; 54(2): 940–954. DOI: 10.1016/j.neuroimage.2010.09.018 [PubMed: 20851199]

17. Wang L, Shi F, Li G, et al. Segmentation of neonatal brain MR images using patch-driven level sets. Neuroimage. 2014; 84:141–158. DOI: 10.1016/j.neuroimage.2013.08.008 [PubMed: 23968736]

18. Wu G, Wang Q, Zhang D, Nie F, Huang H, Shen D. A generative probability model of joint label fusion for multi-atlas based brain segmentation. Med Image Anal. 2014; 18(6):881–890. DOI: 10.1016/j.media.2013.10.013 [PubMed: 24315359]

19. Collins DL, Neelin P, Peters TM, Evans AC. Automatic 3D intersubject registration of MR volumetric data in standardized Talairach space. J Comput Assist Tomogr. 1994; 18(2):192–205. [PubMed: 8126267]

20. Kim JS, Singh V, Lee JK, et al. Automated 3-D extraction and evaluation of the inner and outer cortical surfaces using a Laplacian map and partial volume effect classification. Neuroimage. 2005; 27(1):210–221. DOI: 10.1016/j.neuroimage.2005.03.036 [PubMed: 15896981]

21. Robbins S, Evans AC, Collins DL, Whitesides S. Tuning and comparing spatial normalization methods. Med Image Anal. 2004; 8(3):311–323. DOI: 10.1016/j.media.2004.06.009 [PubMed: 15450225]

22. Boucher M, Whitesides S, Evans A. Depth potential function for folding pattern representation, registration and analysis. Med Image Anal. 2009; 13(2):203–214. DOI: 10.1016/j.media.2008.09.001 [PubMed: 18996043]

23. Eskildsen SF, Coupe P, Fonov V, et al. BEaST: brain extraction based on nonlocal segmentation technique. Neuroimage. 2012; 59(3):2362–2373. DOI: 10.1016/j.neuroimage.2011.09.012 [PubMed: 21945694]

24. Desikan RS, Segonne F, Fischl B, et al. An automated labeling system for subdividing the human cerebral cortex on MRI scans into gyral based regions of interest. Neuroimage. 2006; 31(3):968–980. DOI: 10.1016/j.neuroimage.2006.01.021 [PubMed: 16530430]

25. Mueller SG, Laxer KD, Barakos J, Cheong I, Garcia P, Weiner MW. Widespread neocortical abnormalities in temporal lobe epilepsy with and without mesial sclerosis. Neuroimage. 2009; 46(2):353–359. DOI: 10.1016/j.neuroimage.2009.02.020 [PubMed: 19249372]

26. Gok B, Jallo G, Hayeri R, Wahl R, Aygun N. The evaluation of FDG-PET imaging for epileptogenic focus localization in patients with MRI positive and MRI negative temporal lobe epilepsy. Neuroradiology. 2013; 55(5):541–550. DOI: 10.1007/s00234-012-1121-x [PubMed: 23223825]

27. Wagner J, Weber B, Urbach H, Elger CE, Huppertz H-J. Morphometric MRI analysis improves detection of focal cortical dysplasia type II. Brain. 2011; 134(Pt 10):2844–2854. DOI: 10.1093/brain/awr204 [PubMed: 21893591]

28. Goffin K, Van Paesschen W, Dupont P, et al. Anatomy-based reconstruction of FDG-PET images with implicit partial volume correction improves detection of hypometabolic regions in patients

with epilepsy due to focal cortical dysplasia diagnosed on MRI. Eur J Nucl Med Mol Imaging. 2010; 37(6):1148–1155. DOI: 10.1007/s00259-010-1405-5 [PubMed: 20306037]

29. Rathore C, Dickson JC, Teotónio R, Ell P, Duncan JS. The utility of 18F-fluorodeoxyglucose PET (FDG PET) in epilepsy surgery. Epilepsy Res. 2014; 108:1306–1314. DOI: 10.1016/j.eplepsyres.2014.06.012 [PubMed: 25043753]

30. Greve DN, Salat DH, Bowen SL, et al. Different partial volume correction methods lead to different conclusions: An (18)F-FDG-PET study of aging. Neuroimage. 2016; 132:334–343. DOI: 10.1016/j.neuroimage.2016.02.042 [PubMed: 26915497]

31. Abdulkadir A, Mortamet B, Vemuri P, Jack CRJ, Krueger G, Kloppel S. Effects of hardware heterogeneity on the performance of SVM Alzheimer's disease classifier. Neuroimage. 2011; 58(3):785–792. DOI: 10.1016/j.neuroimage.2011.06.029 [PubMed: 21708272]

32. Colombo N, Tassi L, Deleo F, et al. Focal cortical dysplasia type IIa and IIb: MRI aspects in 118 cases proven by histopathology. Neuroradiology. 2012; 54(10):1065–1077. DOI: 10.1007/s00234-012-1049-1 [PubMed: 22695739]

33. Wang ZI, Jones SE, Jaisani Z, et al. Voxel-based morphometric magnetic resonance imaging (MRI) postprocessing in MRI-negative epilepsies. Ann Neurol. 2015; 77(6):1060–1075. DOI: 10.1002/ana.24407 [PubMed: 25807928]

34. Fauser S, Sisodiya SM, Martinian L, et al. Multi-focal occurrence of cortical dysplasia in epilepsy patients. Brain. 2009; 132(Pt 8):2079–2090. DOI: 10.1093/brain/awp145 [PubMed: 19506069]

35. Palmini A, Gambardella A, Andermann F, et al. Intrinsic epileptogenicity of human dysplastic cortex as suggested by corticography and surgical results. Ann Neurol. 1995; 37(4):476–487. DOI: 10.1002/ana.410370410 [PubMed: 7717684]

36. Mellerio C, Roca P, Chassoux F, et al. The power button sign: a newly described central sulcal pattern on surface rendering MR images of type 2 focal cortical dysplasia. Radiology. 2015; 274(2):500–507. DOI: 10.1148/radiol.14140773 [PubMed: 25243540]

37. Regis J, Tamura M, Park MC, et al. Subclinical abnormal gyration pattern, a potential anatomic marker of epileptogenic zone in patients with magnetic resonance imaging-negative frontal lobe epilepsy. Neurosurgery. 2011; 69(1):80–84. DOI: 10.1227/NEU.0b013e318212bb1a [PubMed: 21346658]

38. Roca P, Mellerio C, Chassoux F, et al. Sulcus-based MR analysis of focal cortical dysplasia located in the central region. PLoS One. 2015; 10(3):e0122252.doi: 10.1371/journal.pone.0122252 [PubMed: 25822985]

39. Blanken LME, Mous SE, Ghassabian A, et al. Cortical morphology in 6- to 10-year old children with autistic traits: a population-based neuroimaging study. Am J Psychiatry. 2015; 172(5):479–486. DOI: 10.1176/appi.ajp.2014.14040482 [PubMed: 25585034]

40. Voets NL, Bernhardt BC, Kim H, Yoon U, Bernasconi N. Increased temporolimbic cortical folding complexity in temporal lobe epilepsy. Neurology. 2011; 76(2):138–144. DOI: 10.1212/WNL.0b013e318205d521 [PubMed: 21148116]

41. Ecker C, Ginestet C, Feng Y, et al. Brain surface anatomy in adults with autism: the relationship between surface area, cortical thickness, and autistic symptoms. JAMA psychiatry. 2013; 70(1):59–70. DOI: 10.1001/jamapsychiatry.2013.265 [PubMed: 23404046]
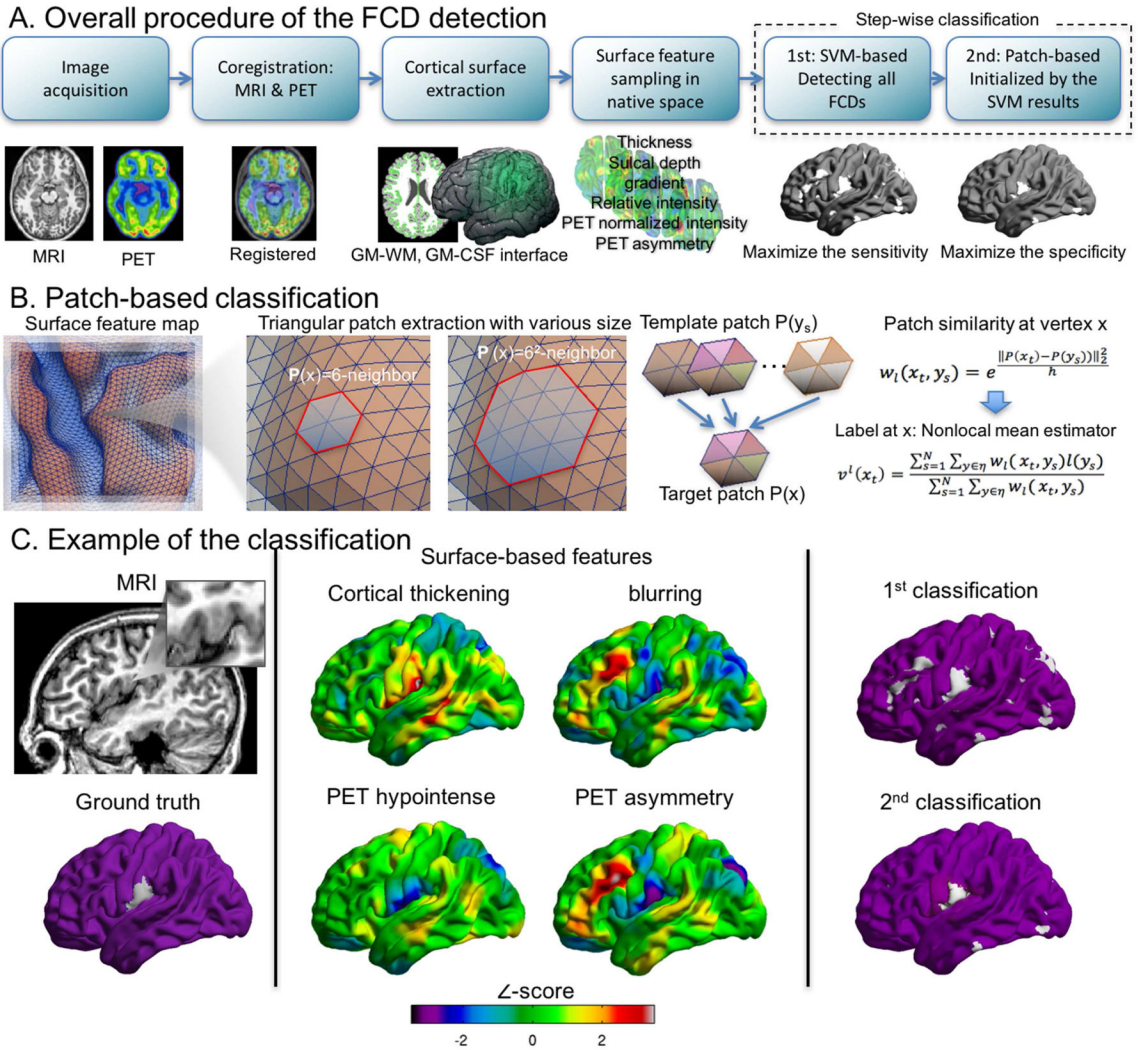
Figure 1.

The lesion classification procedure (**A**), the illustration of the patch-based classification and the result for a MRI-negative case (**C**). In panel **C**, only representative features (z>3) are shown. The classification result shows that the 2nd patch-based classifier cleaned most of the extralesional clusters that were detected in 1st SVM-based classifier, while the 2nd classifier maintained the coverage of the true lesional cluster.
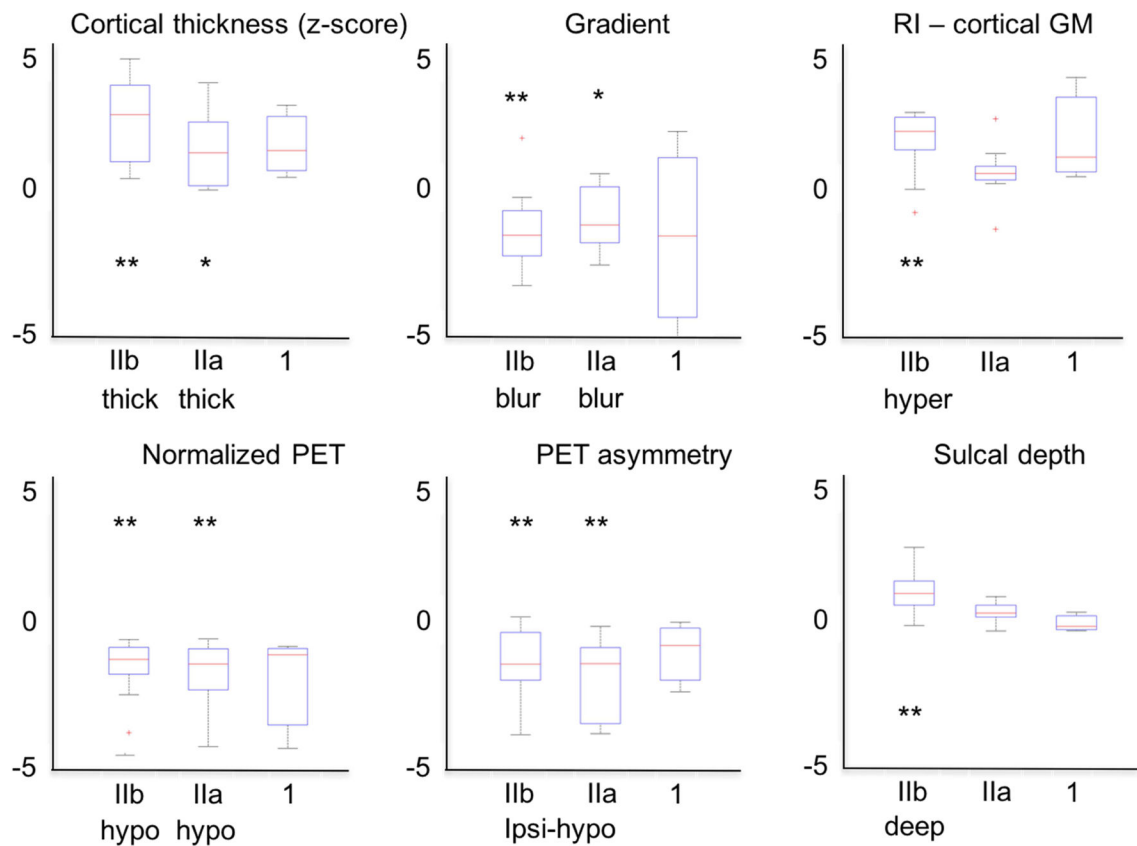
Figure 2.
Feature characteristics of FCD lesions for each histopathological type. The vertex-wise imaging features were normalized with respect to the distribution of the TLE group using z-score transformation. Each feature was averaged within the FCD lesion label. We evaluated the lesion characteristics using the box-whisker plot for each histopathological type of FCD.
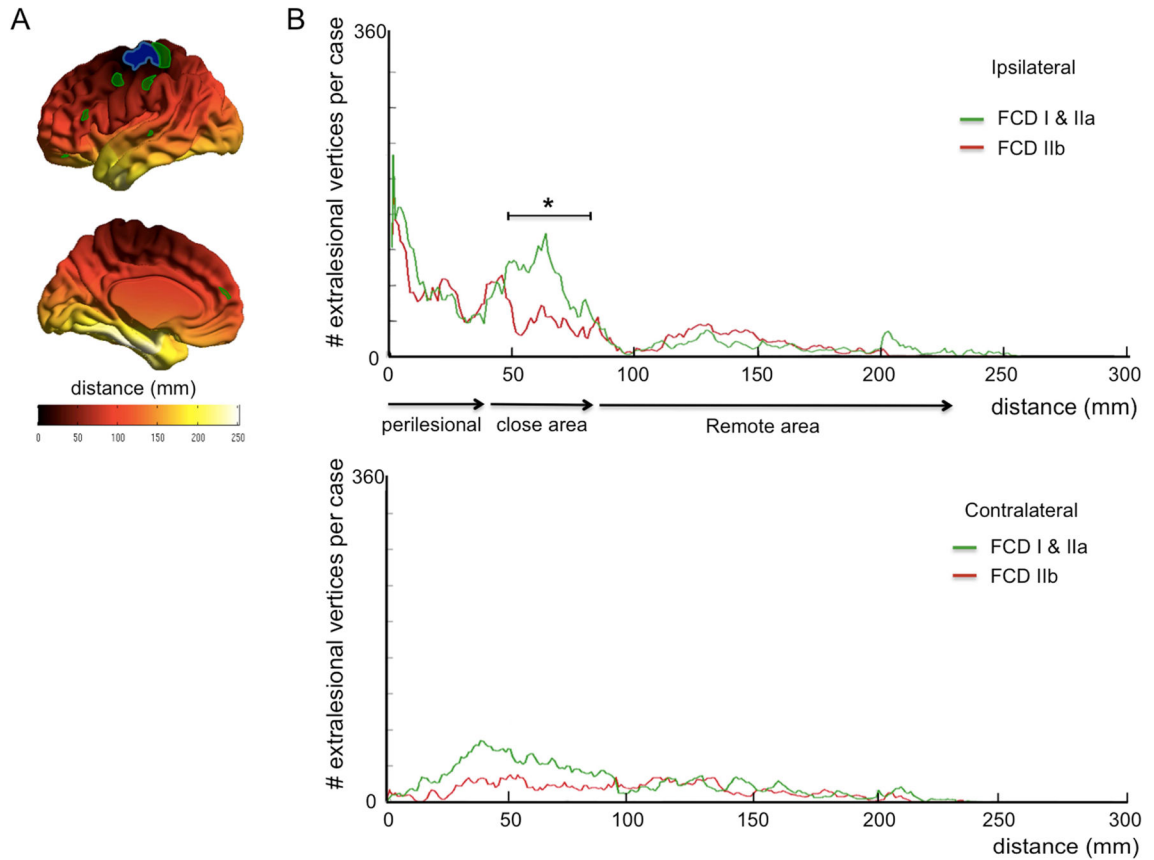
Figure 3.
Distance profiling of extralesional clusters detected using the proposed classifier. **A**) We generated a distance map from the boundary of the primary lesion (blue) using the geodesic distance propagation. We then computed the distance at given vertices detected as "extralesional" (green). **B)** We assessed the number of extralesional vertices per patient identified at the given distance from the FCD lesion. In the close area (40–80mm), patients with FCD type I or IIa (average shown in green) presented a significantly larger number of extralesional abnormalities compared to those with FCD IIb (red).

Table 1

Patient demographics and FCD lesion characteristics

	FCD Patients (n=28)		**TLE Subjects (n=23)**	
Age (mean ± SD years)	26.5 ± 14.1, range 3–52		35.3 ± 12.7, range 14–56	
Gender (%)	15 males (53.6%)		9 males (39.1%)	
Histology (%)	FCD Type I	3 (10.7%)	Gliosis	8 (34.8%)
	FCD Type IIa	11 (39.3%)		
			Mesial Temporal Sclerosis	15 (65.2%)
	FCD Type IIb	14 (50.0%)		
Lesion location (%)	Frontal	19 (67.9%)	N.A.	
	Temporal	4 (14.3%)		
	Temporo-occipital	3 (10.7%)		
	Parietal	2 (7.1%)		
Lesion size (mm^3)	Negative/small (n=18): 977 ± 625 mm^3; range 53–2,389 mm^3		N.A.	
	Larger (n=10): 3770 ± 1574 mm^3; range 2577–7,506 mm^3			

Table 2

The performance of the proposed classifiers. Nonlesional tissues were sampled in MRI-negative TLE patients.

A: 1st step using SVM

	FP rate % (using MRI alone)		FP rate % (MRI + PET)	
	At the best trade-off	At max specificity	At the best trade-off	At max specificity
TLE subjects	2.7±1.7	1.4±1.6	1.7±1.0	0.7±0.8
FCD patients	11.4±11.1	8.0±7.9	16.1±14.1	10.1±8.8
detected lesion	27/28=96%	22/28=79%	28/28=100%	25/28=89%
	#FP cluster		**#FP cluster**	
TLE subjects	29.5±13.5	-	23.5±12.1	-
FCD patients	67.4±26.3	-	63.5±26.5	-
TP coverage	33.3±31.8%	-	39.3±21.6%	-

B: 2nd step using a patch-based analysis

	FP rate % (using MRI alone)		FP rate % (MRI + PET)	
	At max Sensitivity	At max specificity	At max Sensitivity	At max specificity
TLE subjects	0.1±0.1	0.0±0.0	0.0±0. 0	0.0±0.0
FCD patients	2.8±0.8	1.2±0.7	3.8±1.4	2.4±0.8
detected lesion	23/28=82%	17/28=61%	26/28=93%	18/28=64%
	#FP cluster		**#FP cluster**	
TLE subjects	8.0±7.1	0.5±0.7	0.0±0.0	0.0±0.0
FCD patients	26.3±18.8	2.2±2.2	35.8±12.2	2.6±2.0
TP coverage	32.3±25.6%	22.9±17.4%	38.5±20.8%	22.9±17.4%

[*] FP rate = mean of #vertices of FP / #vertices of negative vertices (TN + FN) per individual

[*] Detected lesion = any cluster overlapped with the TP lesional label.

[*] Best trade-off obtained when detecting the maximum number of TP labels with the highest posterior probability of the classifier.

[*] Max specificity obtained at the maximum posterior probability (99%).

Table 3

The performance of the proposed classifiers. Nonlesional tissues were sampled from the extralesional areas in FCD patients.

A: 1st step using SVM

	FP rate % (using MRI alone)		FP rate % (MRI + PET)	
	At the best trade- off	At max specificity	At the best trade- off	At max specificity
TLE subjects	3.0±2.1	1.4±1.9	1.9±1.2	0.9±1.0
FCD patients	7.5±5.0	3.4±3.5	9.6±8.3	5.1±2.8
detected lesion	24/28=86%	20/28=71%	25/28=89%	22/28=79%
	#FP cluster		#FP cluster	
FCD patients	36.4±26.3	-	43.5±19.5	-
TP coverage	20.1±24.3%	-	32.3±17.8%	-
FCD patients	7.1±4.6	3.1±3.1	9.2±7.8	4.7±2.3

B: 2nd step using a patch-based analysis

	FP rate % (using MRI alone)		FP rate % (MRI + PET)	
	At the best trade- off	At max specificity	At the best trade- off	At max specificity
TLE subjects	0.3±0.3	0.1±0.3	0.3±0.2	0.1±0.1
FCD patients	2.1±0.8	0.9±0.6	3.2±1.4	1.9±0.5
detected lesion	20/28=71%	13/28=46%	23/28=82%	14/28=50%
	#FP cluster		#FP cluster	
FCD patients	17.3±14.2	2.0±1.9	24.8±9.7	2.2±1.8
TP coverage	25.3±21.1%		17.4±17.9%	
FCD patients	1.9±0.6	0.8±0.5	3.4±1.2	2.2±0.6

*
FP rate = mean of #vertices of FP / #vertices of negative vertices (TN + FN) per individual

*
Detected lesion = any cluster overlapped with the TP lesional label.

*
Best trade-off obtained when detecting a maximum number of TP labels with the highest posterior probability of the classifier.

*
Max specificity obtained at the maximum posterior probability (99%).

Table 4

Comparison of FCD lesion detection sensitivity across different qualitative and quantitative evaluations

Subjects/ FCD type	Visual MRI	Visual PET	Visual multimodal	Classifier MRI	Classifier PET	Classifier MRI+PET	% Good Surgical Outcomes
Overall	11	10	19	**23**	17	**26**	76.8
(n=28)	(39%)	(35%)	(68%)	**(82%)**	(61%)	**(93%)**	
Type I	1	1	2	2	2	3	66.7
(n=3)	(33%)	(33%)	(67%)	(67%)	(67%)	(100%)	
Type IIa	2	4	4	**8**	7	**10**	72.7
(n=11)	(18%)	(24%)	(24%)	**(72%)**	(64%)	**(91%)**	
Type IIb	8	5	13	13	8	13	90.9
(n=14)	(57%)	(36%)	(93%)	(93%)	(57%)	(93%)	

Visual MRI and visual PET sensitivity as obtained from radiology reports.

Visual Multimodal imaging included the use of MEG, SPECT, and PET-MRI coregistration.

Good surgical outcome is defined as Engel I or II postoperative seizure outcomes.

Bold: Significantly higher sensitivity relative to visual evaluation (Fisher's exact test).